

Provided for non-commercial research and education use.  
Not for reproduction, distribution or commercial use.



This article appeared in a journal published by Elsevier. The attached copy is furnished to the author for internal non-commercial research and education use, including for instruction at the authors institution and sharing with colleagues.

Other uses, including reproduction and distribution, or selling or licensing copies, or posting to personal, institutional or third party websites are prohibited.

In most cases authors are permitted to post their version of the article (e.g. in Word or Tex form) to their personal website or institutional repository. Authors requiring further information regarding Elsevier's archiving and manuscript policies are encouraged to visit:

<http://www.elsevier.com/copyright>



ELSEVIER

available at [www.sciencedirect.com](http://www.sciencedirect.com)journal homepage: [www.elsevier.com/locate/jmbbm](http://www.elsevier.com/locate/jmbbm)

## Research paper

# Characterization of indentation response and stiffness reduction of bone using a continuum damage model

Jingzhou Zhang<sup>a</sup>, Michelle M. Michalenko<sup>a</sup>, Ellen Kuhl<sup>b</sup>, Timothy C. Ovaert<sup>a,\*</sup><sup>a</sup> Department of Aerospace and Mechanical Engineering, University of Notre Dame, Notre Dame, IN 46556, USA<sup>b</sup> Department of Mechanical Engineering, Stanford University, Stanford, CA 94305, USA

## ARTICLE INFO

## Article history:

Received 23 February 2009

Received in revised form

28 July 2009

Accepted 3 August 2009

Published online 11 August 2009

## ABSTRACT

Indentation tests can be used to characterize the mechanical properties of bone at small load/length scales offering the possibility of utilizing very small test specimens, which can be excised using minimally-invasive procedures. In addition, the need for mechanical property data from bone may be a requirement for fundamental multi-scale experiments, changes in nano- and micro-mechanical properties (e.g., as affected by changes in bone mineral density) due to drug therapies, and/or the development of computational models. Load vs. indentation depth data, however, is more complex than those obtained from typical macro-scale experiments, primarily due to the mixed state of stress, and thus interpretation of the data and extraction of mechanical properties is more challenging. Previous studies have shown that cortical bone exhibits a visco-elastic response combined with permanent deformation during indentation tests, and that the load vs. indentation depth response can be simulated using a visco-elastic/plastic material model. The model successfully captures the loading and creep displacement behavior, however, it does not adequately reproduce the unloading response near the end of the unloading cycle, where a pronounced decrease in contact stiffness is observed. It is proposed that the stiffness reduction observed in bone results from an increase in damage; therefore, a plastic-damage model was investigated and shown capable of simulating a typical bone indentation response through an axisymmetric finite element simulation. The plastic-damage model was able to reproduce the full indentation response, especially the reduced stiffness behavior exhibited during the latter stages of unloading. The results suggest that the plastic-damage model is suitable for describing the complex indentation response of bone and may provide further insight into the relationship between model parameters and mechanical/physical properties.

© 2009 Elsevier Ltd. All rights reserved.

\* Corresponding address: Department of Aerospace and Mechanical Engineering, University of Notre Dame, 146 Multidis. Research Bldg., Notre Dame, IN 46556, USA. Tel.: +1 574 631 9371; fax: +1 574 631 2144.  
E-mail address: [tovaert@nd.edu](mailto:tovaert@nd.edu) (T.C. Ovaert).

## 1. Introduction

Damage causes a progressive degradation of material continuity, which distinguishes it from other types of inelastic material behavior (Kachanov, 1958; Lemaitre and Chaboche, 1990). The loss of integrity can have an adverse effect on mechanical properties, and can be attributed to microscopic cracks and/or voids. Continuum damage theories have been applied to indentation and contact mechanics of various materials, including metals, ceramics, glass, paper, and ice (Lee et al., 2006a,b, 2008; Sun and Khaleel, 2004; Sun et al., 2005; Hägglund and Isaksson, 2007; Licht et al., 2003; Das et al., 2009).

Bone tissue, as a composite material, contains initial voids and other non-homogeneities (Frost, 1960) that are naturally occurring and distinct from damage. However, when subjected to mechanical loading, such as indentation, damage accumulation may occur. Numerous investigations have been performed, seeking to characterize damage in bone based on property degradation via histological observations as well as acoustic emission (Kohn, 1995; Enoki and Kishi, 1991; Wright et al., 1981; Fischer et al., 1986; Inoue et al., 1986; Jonsson and Eriksson, 1984). Keaveny et al. (1994) measured the changes in modulus and strength for bovine trabecular bone loaded in compression to various strains beyond its elastic range, and found that modulus was reduced for all applied strains, whereas strength was reduced only for certain strain levels; thus the modulus was always reduced more than strength. These results agree with those for cortical bone in tensile loading, supporting the conclusion that the damage behavior of cortical and trabecular bone is similar for low strains.

Archdeacon et al. (1996) investigated the relationship between loading rate, relaxation time, and damage accumulation in torsion for bovine cortical bone, showing that rate dependent reductions in strength are due to time dependent damage accumulation, and that damage accumulates nonlinearly with time. Jepsen and Davy (1997) studied the damage process on human cortical bone specimens subjected to a series of torsional relaxation cycles, and determined the effects of damage on the elastic, yield, viscous, and failure properties of cortical bone. Vashishth et al. (2002) performed bending tests to obtain the effects of damage morphology on bone fragility by determining the relationships between damage morphology, nano-indentation properties, and fatigue behavior of bone. They noted that bone tends to form organized linear micro-cracks, not diffuse damage, which contributes to bone quality, and also gave evidence for different stiffness changes in younger and older bone specimens responding to fatigue. Diffuse damage, however, may occur during small-scale indentation tests due to damage to the mineral-mineral and mineral-collagen network. Kotha and Guzelsu (2003) conducted tensile tests on bovine bone samples to characterize the effects of damage on the mechanical behavior of decalcified samples and bone tissue, and suggested that damage in bone is caused by shear failure of the organic matrix.

In addition to the aforementioned experimental studies, damage models for bone have also been proposed. Ramtani and Zidi (2001) developed a theoretical model of the competition between damage and internal remodeling,

and derived a damage force that defines the onset of damage and drives damage propagation. Niebur et al. (2000, 2001) developed a non-linear high-resolution finite element analysis technique for failure analysis of trabecular bone and assessed the sensitivity of tissue level yielding to the assumed tissue yield properties and apparent loading conditions. Additional models have been developed addressing damage accumulation (Carter and Caler, 1985), changes in strength and stiffness after fatigue loading (Carter and Hayes, 1977), remodeling (Hart et al., 1984), the extent of bone ossification during loading (Prendergast and Huiskes, 1996), and cyclic overloads (Garcia et al., 2009).

Damage accumulation is a normal response of composite materials to mechanical loading. It is this damageability that contributes to the superior fatigue resistance and toughness of composite materials compared to monolithic materials (Reifsnider, 1991). In bone, the presence of damage also has a biological consequence. Since micro-cracks exist at some volume in normal, healthy bone, they may play a role in the turnover process as well as adaptive behavior (Martin and Burr, 1982). Histological evidence indicates that damage occurs at the micro-structural level. Elastic-plastic finite element simulations of bone indentation have been performed (Zhang et al., 2008; Ovaert et al., 2003; Wang and Ovaert, 2009; Fan et al., 2004; Tai et al., 2006; Mullins et al., 2009), however, the incorporation of continuum damage mechanics as a result of indentation has received little if any attention. Thus, the ability to simulate the indentation behavior of bone and to parameterize its damage response during indentation may provide greater insight into its small-scale deformation mechanics, remodeling, changes in diffusivity and conductivity, and ultimately its potential response to drug therapies. The objective of this paper, therefore, is to model the indentation behavior of bone using a plastic-damage model, and to assess the application of the model parameters to the study of bone tissue mechanics.

## 2. Materials and methods

### 2.1. Materials and experiments

The experimental and test specimen details have been discussed previously in Zhang et al. (2008). Two bone specimens approximately  $15 \times 8 \times 2$  mm thick were dissected from monkey vertebrae. The first was placebo-treated and sham-ovariectomized. The second was placebo-treated and ovariectomized, both from female cynomolgus monkeys. Additional details on the monkey specimens may be found elsewhere (Lees et al., 2002). All specimens were dehydrated in a series of alcohol baths and embedded in epoxy resin at room temperature; and subjected to the same cleaning and mounting protocol, and polished using silicon carbide abrasive papers and diamond paste to an approximate (center-line-average,  $R_a$ ) surface roughness of 0.05  $\mu\text{m}$ , necessary for repeatable indentation results. Taguchi orthogonal arrays were used to design the experimental test matrix. A typical load vs. indentation depth curve (100 mN maximum load, 50 mN/s loading/unloading rate, 10 s hold time) along with an optimized

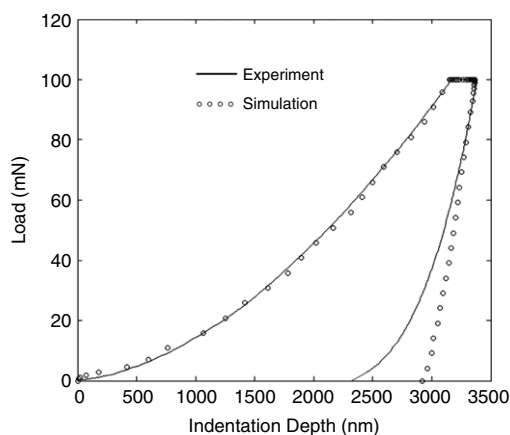


**Fig. 1 – Experimental indentation data and four-parameter finite element model simulation.**

fit from the four-parameter visco-elastic/plastic model discussed in Zhang et al. (2008) is shown in Fig. 1. Note that the four-parameter model, a modified Kelvin–Voigt model incorporating a linear dashpot in parallel with a Ramberg–Osgood (elastic–plastic spring) strain decomposition, closely simulates the loading, creep, and initial unloading slope (a visco-elastic event), however, near the end of the unloading cycle, as the bone stiffness decreases, the simulation error increases. This phenomenon is not a result of tip-surface contamination or other test artifact, and most notably has been observed by others when indenting bone (Tai et al., 2005; Pelled et al., 2007; Hoffler et al., 2005).

In order to further investigate the results from the damage model simulations, additional bovine cortical bone indentation tests were performed. Bovine cortical bone was used since it was not possible to cross-section the original monkey specimens (Zhang et al., 2008). Samples of cortical bone from the mid-diaphysis of a bovine tibia were harvested and machined into rectangular test specimens  $15\text{ mm} \times 17\text{ mm} \times 5\text{ mm}$  using a diamond saw (Buhler Inc., Lake Bluff, IL). The specimens were then cut in half (length-wise), and adhered (cyanoacrylate adhesive) to the lapped and polished surface of a 25 mm diameter steel washer, butting the two saw-cut faces together as closely as possible. Due to the saw cutting process, the faces incur a finite edge “radius” on the order of  $10\text{ }\mu\text{m}$ . Thus, the near-surface gap of the two halves was approximately  $20\text{ }\mu\text{m}$ . The nanoindenter tip radius is much smaller ( $0.1\text{ }\mu\text{m}$ ), thus, a larger tip was used, at a higher applied load, in order to negate the effects of the near-surface gap. This prohibited an exact comparison to the damage model predictions, however, it did enable a qualitative examination of the damage field in the subsurface indent zone. This procedure was followed, rather than indentation followed by polishing until the cross-section of an indented region was exposed, since polishing could result in additional non-indentation-related damage to occur, overshadowing the damage induced by indentation alone.

Prior to testing, specimens were thawed for a 12 h period, then submerged in a 20 mL solution of 0.0005 M alizarin red stain, and stored under vacuum for 24 h in order to label any pre-existing damage. Indentation tests were then performed using a  $250\text{ }\mu\text{m}$  radius (approximate) conospherical

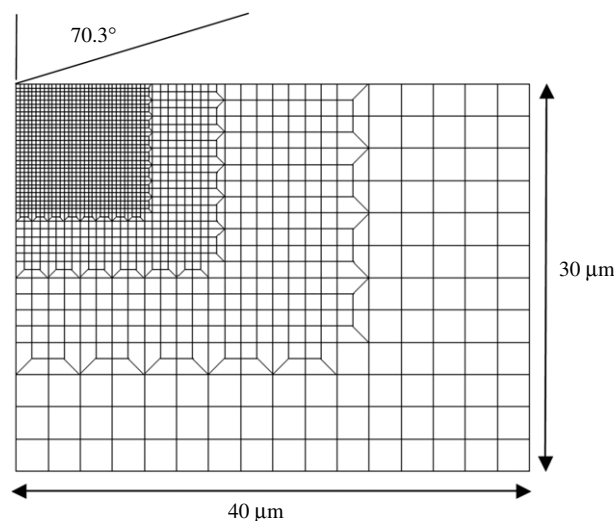


**Fig. 2 – Mesh used in the finite element simulations.**

tip, at an applied normal load of 14 N. Following indentation, specimens were stored under vacuum for 12 h, and then submerged in a 20 mL solution of 0.0005 M calcein stain, which labeled any microcracks and diffuse damage that occurred due to indentation. The bone was then sectioned into 0.5 mm thick wafers, and the indent cross sections were examined using fluorescence microscopy (O’Brien et al., 2003).

## 2.2. Finite element simulation

The plastic-damage model applied in this work is based on the notion that elastic stiffness degradation is isotropic, embedded in the plasticity model, and characterized by a scalar damage variable, as proposed by Lubliner et al. (1989) and Lee and Fenves (1998). Numerous other damage models have been proposed (see Grassl and Jirasek (2006), Contrafatto and Cuomo (2006), and Menzel et al. (2005) for example), especially for analysis of the failure of quasi-brittle materials such as concrete. The model is implemented within the ABAQUS<sup>TM</sup> finite element solver, and is primarily intended to provide a general capability for the analysis of concrete structures and other quasi-brittle bone-like materials such as concrete. The main failure mechanisms for this model are cracking in tension and crushing in compression. Based on the notion that bone is quasi-brittle, having certain material characteristics such as micro-structural heterogeneities (pores, micro-cracks, etc.), different failure strengths in tension and compression, and strain rate sensitivity (Hansen et al., 2008), an attempt was made to apply the aforementioned plastic-damage model to bone indentation data. An axisymmetric (rigid)  $140.6^\circ$  conical indenter was used to model the diamond indenter since it approximates the Berkovich shape with the same projected area-to-depth ratio. A typical mesh consisted of approximately 1800 axisymmetric 4-node elements, as seen in Fig. 2.

## 2.3. Plastic-damage model

The plastic-damage model of Lubliner et al. (1989) and Lee and Fenves (1998) assumes that damage progresses under

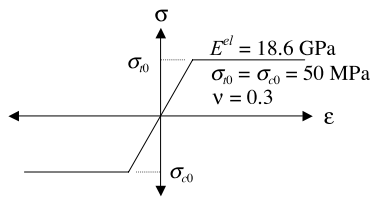


**Fig. 3 – Symmetric material model used to assess relative strain contributions in blunt indentation. Yield stress in compression/tension = 50 MPa, Poisson's ratio = 0.3.**

both compressive and tensile loading. In blunt indentation, however, tensile cracking is typically locally restricted to narrow bands at the contact edge. Accordingly, its contribution to the reduction in the overall load carry capacity is assumed to be of minor order and damage is attributed exclusively to compression. Attributing stress-strain constitutive behavior to a material's compression response, in the context of sharp indentation (e.g., blunt cones, Vickers, and Berkovich), has also been noted by Dao et al. (2001) and Chollacoop et al. (2003). In order to test this hypothesis, the equivalent plastic strains in compression and tension were determined using an elastic/perfectly-plastic symmetric material test model, as shown in Fig. 3. In Fig. 4(a), one can see that the equivalent plastic compressive strains are located beneath the indenter. The unusually large values immediately beneath the tip of the indenter are due to the singularity at the (sharp) punch tip. On the other hand, the equivalent plastic tensile strains (Fig. 4(b)) are localized near the edge of contact (where they exhibit only a small influence at the beginning of the unloading period) and they are approximately one order of magnitude lower than their compressive counterpart. Therefore, based on these results, damage behavior was attributed exclusively to compressive loading. In what follows, we will briefly summarize the constitutive equations of elasto-plastic damage for cohesive frictional materials based on the model of Lubliner et al. (1989) refined by Lee and Fenves (1998).

With the assumption of geometrically linear kinematics, the strain tensor  $\epsilon$  can be additively decomposed into an elastic and a plastic part:

$$\epsilon = \epsilon^{el} + \epsilon^{pl} \quad \text{with } \epsilon = \nabla^{sym} \mathbf{u}. \quad (1)$$

Following the classical effective stress concepts of continuum damage theory, the effective stress  $\bar{\sigma} = \mathbf{E}^{el} : [\epsilon - \epsilon^{pl}] = \sigma/[1 - d]$  corresponds to the true stress  $\sigma$  weighted by the undamaged area fraction  $[1 - d]$ . Here,  $d$  is the scalar damage variable for isotropic damage with  $1 \geq d \geq 0$  where  $d = 0$  defines the undamaged state while  $d = 1$  indicates the complete loss of material integrity. The stresses of the elasto-plastic damage model then follow as:

$$\sigma = [1 - d]\mathbf{E}^{el} : [\epsilon - \epsilon^{pl}] \quad (2)$$

where  $\mathbf{E}^{el}$  is the elasticity tensor parameterized in terms of Young's modulus  $E$  and Poisson's ratio  $\nu$ , which were set at 18.6 GPa (Zysset et al., 1999) and 0.3, respectively.

The elastic domain is bounded by a hyperbolic Drucker-Prager type yield function  $F$ :

$$F = \bar{q} - 3\alpha\bar{p} - Y \leq 0. \quad (3)$$

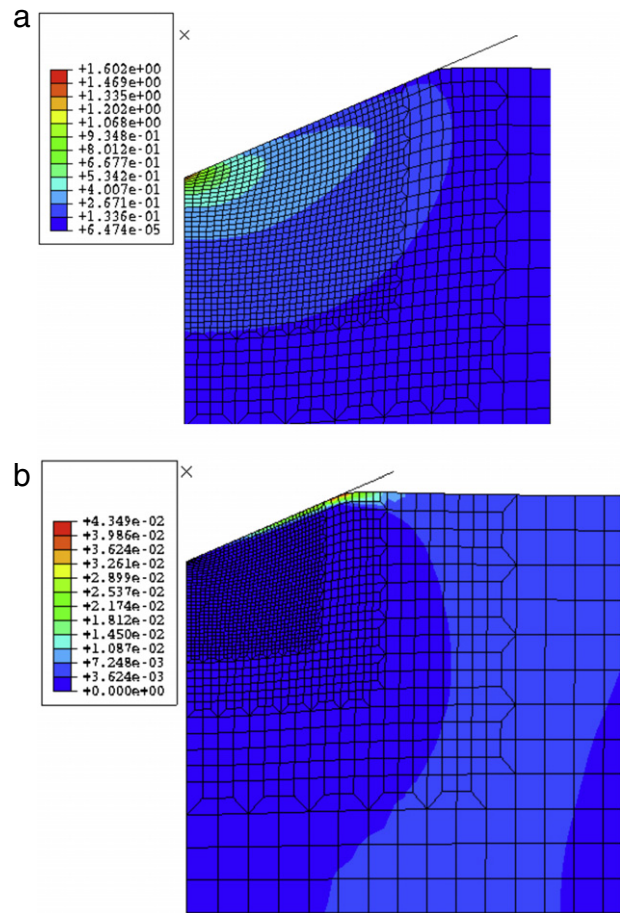


**Fig. 4 – Contours of equivalent plastic strain,  $\kappa_c$ , symmetric material model, (a) equivalent plastic compressive strain, (b) equivalent plastic tensile strain.**

Here,  $\bar{p} = 1/3\bar{\sigma} : I$  is the effective hydrostatic pressure and  $\bar{q} = \sqrt{(3/2)\bar{\sigma}^{dev} : \bar{\sigma}^{dev}}$  is the effective equivalent von Mises stress expressed in terms of the effective deviatoric stress  $\bar{\sigma}^{dev} = \bar{\sigma} - \bar{p}I$ . Plastic hardening is reflected through the yield stress  $Y$ :

$$Y = [1 - \alpha]\bar{\sigma}_c - [(1 - \alpha)\bar{\sigma}_c/\bar{\sigma}_t - [1 + \alpha]](\bar{\sigma}_{max}) \quad (4)$$

which is a function of the effective uniaxial tensile and compressive failure stresses,  $\bar{\sigma}_c$  and  $\bar{\sigma}_t$ , respectively, and of the maximum eigenvalue,  $\bar{\sigma}_{max}$ , of the effective stress  $\bar{\sigma} = \mathbf{E}^{el} : [\epsilon - \epsilon^{pl}]$ . Here,  $(\circ) = 1/2[|\circ| + \circ]$  are the Macaulay brackets, such that under plain compressive loading with  $\bar{\sigma}_{max} < 0$  the second term vanishes and the yield stress simply reduces to  $Y = [1 - \alpha]\bar{\sigma}_c$ . The size of the failure surface is governed by the coefficient,  $\alpha$ :

$$\alpha = \left[ \frac{\sigma_{b0}}{\sigma_{c0}} - 1 \right] / \left[ 2 \frac{\sigma_{b0}}{\sigma_{c0}} - 1 \right] \quad (5)$$

which can be expressed in terms of the ratio of the equibiaxial and uniaxial compressive yield stress  $\sigma_{b0}/\sigma_{c0}$ . The constant  $\sigma_{b0}$  is obtained when two of the principal stresses are equal; for example, in the triaxial confined compression test, where a cylindrical test specimen (compressed along its major axis) is submerged in a confined fluid under pressure.

At high pressure, particularly for materials such as concrete and soils,  $\sigma_{b0}$  can exceed  $\sigma_{c0}$ , the nominal (or unconfined) compressive yield stress, due to a “strengthening” effect from the confinement pressure. Following Lubliner et al. (1989), we choose a  $\sigma_{b0}/\sigma_{c0} = 1.125$ , thus  $\alpha = 0.1$ . The set of equations is complemented by the Kuhn–Tucker conditions  $F\dot{\lambda} = 0$ ,  $\dot{\lambda} \geq 0$ , and  $F \leq 0$  and the consistency conditions  $\dot{F} = 0$ . Cohesive frictional materials such as bone display a non-associated plastic flow defined through a plastic potential,  $G$ , which is assumed to be of hyperbolic Drucker–Prager type, given by:

$$G = \bar{q} - \bar{p} \tan \psi. \quad (6)$$

Again,  $\bar{p}$  and  $\bar{q}$  are the effective hydrostatic pressure and the effective equivalent von Mises stress, respectively, and  $\psi$  denotes the dilation angle. This angle represents the volume change during (non-associated) plastic flow. In general, smaller angles are associated with softer materials, and the opposite for harder materials. Following Lubliner et al. (1989), the dilation angle generally ranges from  $15^\circ$  to  $30^\circ$ , and based on similar values for bone in the literature (Phillips et al., 2003), we chose a value of  $22.5^\circ$  in our simulations. The evolution of the plastic strains  $\epsilon^{pl}$  is governed through the flow rule:

$$\dot{\epsilon}^{pl} = \dot{\lambda} \frac{\partial G}{\partial \sigma}. \quad (7)$$

The evolution of damage  $d$  and the effective uniaxial tensile and compressive failure stresses  $\bar{\sigma}_c$  and  $\bar{\sigma}_t$  are governed by the equivalent plastic strain  $\kappa_c$  and  $\kappa_t$  in compression and tension, respectively.

$$d = d(\kappa_c); \quad \bar{\sigma}_c = \bar{\sigma}_c(\kappa_c); \quad \text{and} \quad \bar{\sigma}_t = \bar{\sigma}_t(\kappa_t). \quad (8)$$

In tension and compression,  $\kappa_c$  and  $\kappa_t$  evolve with respect to the minimum and maximum eigenvalue of the plastic strain  $\epsilon_{\min}^{pl}$  and  $\epsilon_{\max}^{pl}$ , respectively. They take the maximum absolute value that the corresponding eigenvalue has obtained throughout the entire loading history as:

$$\kappa_c = -[1 - r] \min\{\epsilon_{\min}^{pl}\}; \quad \text{and} \quad \kappa_t = r \max\{\epsilon_{\max}^{pl}\} \quad (9)$$

which implies that  $\kappa_c$  and  $\kappa_t$  can never decrease. Obviously, the stress weight factor

$$r = \frac{\sum_{I=1}^3 \langle \bar{\sigma}_I \rangle}{\sum_{I=1}^3 |\bar{\sigma}_I|} \quad (10)$$

is equal to one if all principal stresses  $\sigma_I$  are positive, and is equal to zero if they are all negative. Finally, we apply a visco-plastic regularization of Duvaut–Lions type for the equivalent plastic strains  $\kappa_c$  and  $\kappa_t$  and for the damage variable  $d$ .

$$\begin{aligned} \dot{d}^{vp} &= [d - d_{vp}]/\mu; \quad \dot{\kappa}_c^{vp} = [\kappa_c - \kappa_c^{vp}]/\mu; \quad \text{and} \\ \dot{\kappa}_t^{vp} &= [\kappa_t - \kappa_t^{vp}]/\mu. \end{aligned} \quad (11)$$

Here, we have introduced the viscosity parameter  $\mu$ , which represents the relaxation time of the visco-plastic ( $vp$ ) material;  $d$ ,  $\kappa_c$ , and  $\kappa_t$  correspond to the inviscid case. In the limit of small  $\mu$ , i.e., as  $t/\mu \rightarrow \infty$ , the solution of the visco-plastic system relaxes to the inviscid case.

A simplified compressive stress–strain representation of the key parameters in the plastic damage model may be seen in Fig. 5. Note that the model also assumes that damage initiates after the compressive yield stress occurs. Thus, the simulations do not account for any initial damage state or damage initiation during the elastic loading regime.

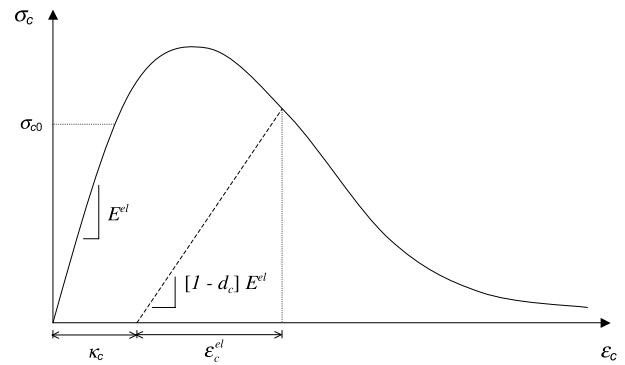


Fig. 5 – Typical stress–strain behavior for quasi-brittle material in compression.

### 3. Results

#### 3.1. Fit to experimental data

As noted in the previous section, several parameters were chosen based on suggested values in Lubliner et al. (1989). By doing this, we can assess the general applicability of the plastic-damage model as a potential tool for representation of bone indentation data. When fitting the model to the experimental data, an integral step is the creation of a representative function which relates the scalar damage variable,  $d_c$ , to the equivalent plastic strain,  $\kappa_c$ , as well as the selection of the post-yield plastic hardening curve after the initial compressive yield stress,  $\sigma_{c0}$ , is reached. Based on the results of Niebur et al. (2001), which showed only a small increase in post- $\sigma_{c0}$  compressive stress (approximately 2%), we assumed perfect plasticity in compression, and set  $\sigma_{c0}$  equal to 100 MPa, which is representative of published data for macro-scale tests (Hansen et al., 2008).

The damage evolution equation couples the equivalent plastic strain to the field equations. In general, damage accumulation can occur under elastic deformation (fatigue), elastic–plastic deformation (ductile plastic damage), or under creep conditions (creep damage). In more complex cases,  $d$  can assume the form of a vector function or fourth order tensor (Kachanov, 1986). Here, we assume the simple case where  $d$  is a scalar function of the equivalent plastic strains. Several functional representations for this evolution equation have been proposed for ductile and brittle materials. For example,

$$d_c(\kappa_c) = 1 - \frac{\kappa_i}{\kappa_c} \frac{\kappa_0 - \kappa_c}{\kappa_0 - \kappa_i} \quad (12)$$

represents a linear damage evolution equation governed by  $\kappa_i$ , the threshold equivalent plastic strain for damage initiation, and  $\kappa_0$ , the limiting equivalent plastic strain in the fully damaged state. Another form,

$$d_c(\kappa_c) = 1 - \frac{\kappa_i}{\kappa_c} \left[ (1 - \gamma) + \gamma e^{-\beta(\kappa_c - \kappa_i)} \right] \quad (13)$$

represents an exponential decay in stiffness, governed by two additional parameters  $\gamma$  and  $\beta$ . Since we assume that damage does not exist at zero equivalent plastic strain, a modified two-parameter exponential equation of the form,

$$d_c(\kappa_c) = \gamma(1 - e^{-\beta\kappa_c}) \quad (14)$$

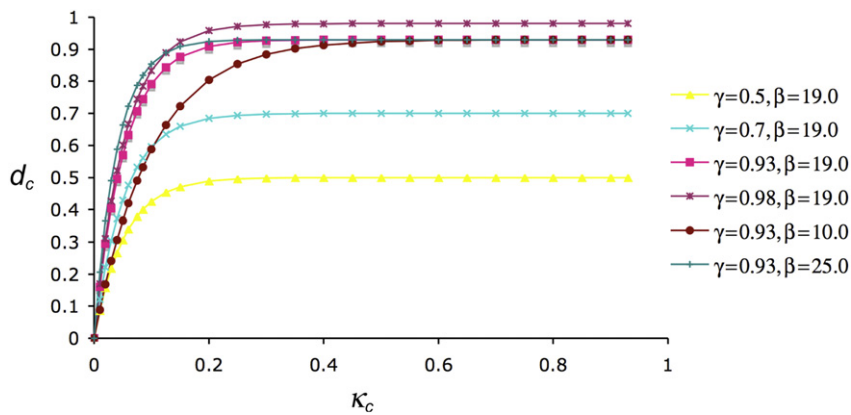


Fig. 6 – Scalar damage variable,  $d_c$ , as a function of the equivalent plastic strain,  $\kappa_c$ , for various values of  $\gamma$  and  $\beta$ .

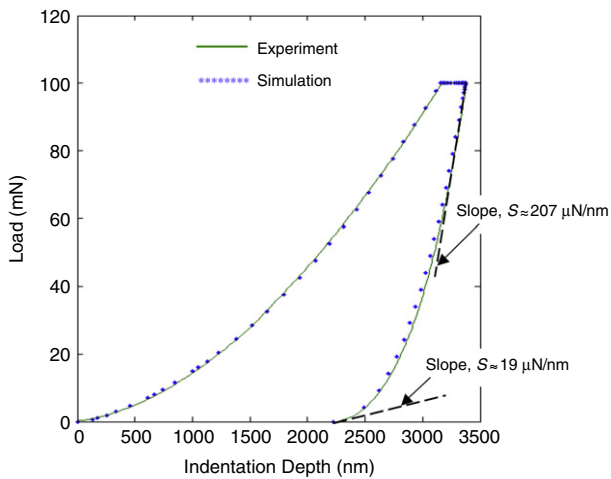


Fig. 7 – Experimental indentation data and plastic-damage model simulation, parameter values from Table 1.

was used to model the damage evolution for bone. In this equation,  $\gamma$  represents the limiting value of  $d_c$  while  $\beta$  governs the rate at which  $d_c$  approaches this limiting value. The shape of Eq. (14) suggests that in bone, damage increases quickly at relatively low  $\kappa_c$  ( $<0.10$ ), and then tends to level off for higher values of  $\kappa_c$ . This suggests that damage is likely to initiate early in the loading cycle, especially near the indenter tip. A range of  $\gamma$  and  $\beta$  values input to Eq. (14) may be seen plotted in Fig. 6.

Using the collective results of the fitted parameter values listed in Table 1, the plastic-damage model can closely simulate a typical bone micro-indentation experimental curve, as shown in Fig. 7. Note that the model fits all stages: loading, holding, as well as initial and final unloading.

Fig. 8 shows a contour plot of the scalar damage variable,  $d_c$ , at the point of maximum indentation depth. The plot of  $d_c$  follows a typical distribution of subsurface shear stress contours beneath a cylindrical or spherical indenter as noted in Johnson (1985).

The plastic-damage model was also used to correlate the measured stiffness reduction, which is prominent characteristic of the unloading curve in Fig. 1. With the parameter set from Table 1, one may plot  $d_c$ , at the end of

Table 1 – Plastic damage model parameters and description.

Parameter	Value (used to fit Fig. 7)	Description
$\psi$	22.5	Dilation angle (degrees)
$\sigma_{b0}/\sigma_{c0}$	1.125	Ratio of the equibiaxial compressive yield stress to the uniaxial compressive yield stress
$\sigma_{c0}$	100	Uniaxial compressive yield stress (MPa)
$E^{el}$	18.6	Young's modulus (GPa) (Fig. 5)
$\mu$	0.04	Relaxation time (s)
$\gamma$	0.93	Constant in Eq. (14)
$\beta$	19.0	Constant in Eq. (14)
$\nu$	0.30	Poisson's ratio

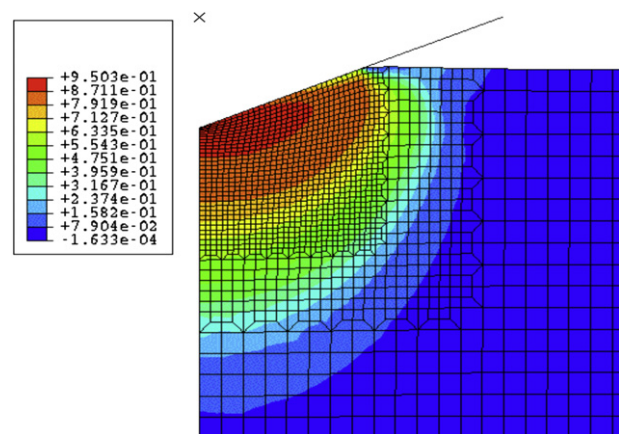
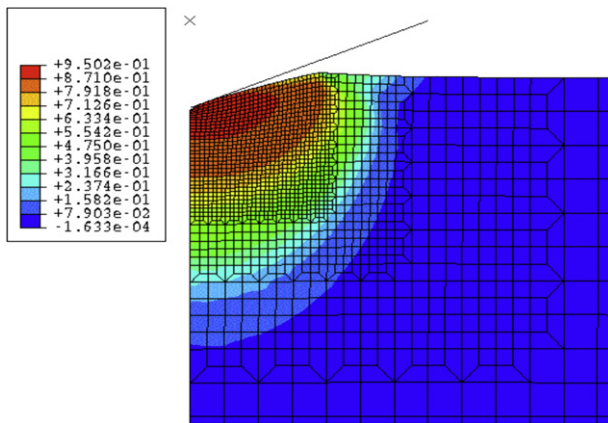


Fig. 8 – Contours of scalar damage variable,  $d_c$ , at maximum indentation load and depth.

the unloading curve, as shown in Fig. 9. For indentation (see also Fig. 5),

$$\text{Modulus} \propto \frac{\sqrt{\pi}}{2} \frac{S}{\sqrt{A_c}} \approx [1 - d_c]E^{el}. \quad (15)$$

Thus, the modulus is proportional to the unloading stiffness, and based on the plastic-damage model, also proportional to  $d_c$ . In Fig. 7, the measured initial and final



**Fig. 9 – Contours of scalar damage variable,  $d_c$ , at the end of unloading.**

stiffness values are 207 and 19  $\mu\text{N}/\text{nm}$ , respectively, which represents a reduction of approximately 90%.

A typical indent cross section on bovine cortical bone, partitioned along the centerline of the indenter axis, can be seen in Fig. 10. Calcein stain labeling is most prevalent in the region beneath the indenter tip, in qualitative agreement with the damage zone prediction in Fig. 9.

### 3.2. Investigation of model parameters

In order to visualize the effects of changes in the parameter values on the load vs. indentation depth simulation, the parameter values were varied individually. The results can be seen in Figs. 11–13. Fig. 11(a) shows the effect of changing the dilation angle,  $\psi$ , and one can see that larger values of  $\psi$  increase the slope of the loading curve, decrease the final indentation depth, and increase the creep displacement. In Fig. 11(b), the effect of changing the  $\sigma_{b0}/\sigma_{c0}$  ratio is shown. Larger values of  $\sigma_{b0}/\sigma_{c0}$  increase the slope of the loading curve, decrease the final indentation depth, and have a negligible effect on the creep displacement.

Fig. 12(a) shows the effect of changes in the compressive yield stress,  $\sigma_{c0}$ . As  $\sigma_{c0}$  increases, the slope of the loading curve increases, and the creep displacement and final indentation depth decrease. Fig. 12(b) shows the effect of increasing Young's modulus,  $E^{\text{el}}$ . As the modulus increases, the slope of the loading curve increases, the creep displacement increases, and the final indentation depth remains relatively unchanged.

Fig. 13(a) shows the effect of changing the relaxation time parameter,  $\mu$ . As  $\mu$  increases, the loading slope and creep displacement also increase. The final indentation depth is relatively unaffected. Fig. 13(b) shows the effect of parameter changes in the damage evolution equation (Eq. (14), and from Fig. 6). As  $\gamma$  increases at constant  $\beta$ , the slope of the loading curve and final indentation depth decrease, and the creep displacement remains relatively unchanged. As  $\beta$  increases at a constant  $\gamma$ , the slope of the loading curve decreases, the creep displacement remains relatively unchanged, and the final indentation depth decreases slightly.

The sensitivity of the damage model parameters was also investigated, to determine which parameters had the

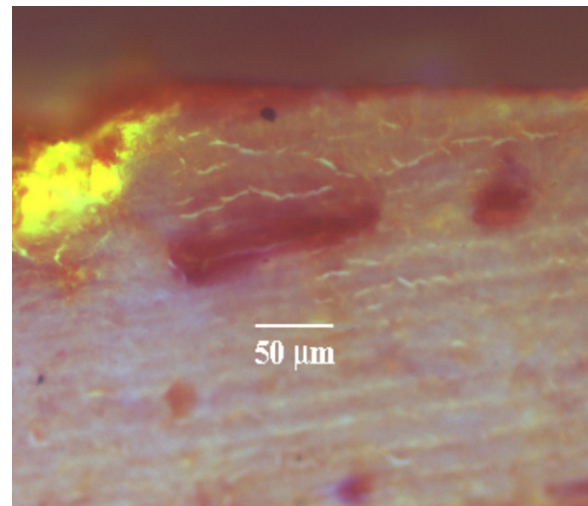


**Fig. 10 – Bovine cortical bone specimen revealing calcein stain labeling after indentation. One-half of indentation zone cross section shown in upper left corner, revealing similarities to the plot of  $d_c$  in Fig. 9.**

largest effect on the indentation simulation. Performing a sensitivity analysis on creep indentation can assume various forms. For example, one can compare the entire simulation curve with the entire experimental curve (loading, holding, and unloading), and compute an overall error (e.g.,  $R^2$  or similar) value. However, two simulations could potentially have the same  $R^2$  value, yet display very different behaviors over the full loading path. For this reason, we chose to perform the sensitivity analysis by examining four important characteristics of a typical indentation curve: the initial indentation depth at maximum load (IID), the total creep displacement during the holding period (TCD), the final indentation depth at zero load (FID), and the final unloading slope (FS). Each of the seven parameters listed in Table 1 (excluding Poisson's ratio, which was fixed at 0.3) was varied approximately  $\pm 50\%$ , with the exception of  $\sigma_{b0}/\sigma_{c0}$  (since ratios less than one are unrealistic) and  $\gamma$  (maximum value equal to one) from the fitted values noted in Table 1. The percent change in the individual curve characteristics was then computed as a function of the percent change in the individual parameters. The results can be seen in Figs. 14 and 15.

Fig. 14(a) shows the sensitivity of the IID to the simulation parameters. It can be seen that this characteristic is (non-linearly) sensitive to all parameters, though to a lesser extent for  $\psi$ ,  $\beta$ , and  $\mu$ . For these three parameters, changes of  $\pm 45\%$  lead to roughly a 5% change in the IID. The parameters with the largest effect are  $\sigma_{b0}/\sigma_{c0}$ ,  $\sigma_{c0}$ ,  $\gamma$ , and  $E^{\text{el}}$ . Increasing  $\sigma_{b0}/\sigma_{c0}$  has a very strong effect, as it elevates the "effective" compressive yield stress under confined compression, which creates a stiffening effect during loading. Similarly, as one decreases the compressive yield stress, the IID increases, since plastic deformation (which has a softening effect) occurs sooner during loading. In addition, decreasing  $\gamma$  decreases the IID. This is due to the nature of Eq. (14). With a smaller value of  $\gamma$ , the final value of  $d_c$  will also decrease; thus, a lesser amount of damage occurs, which effectively

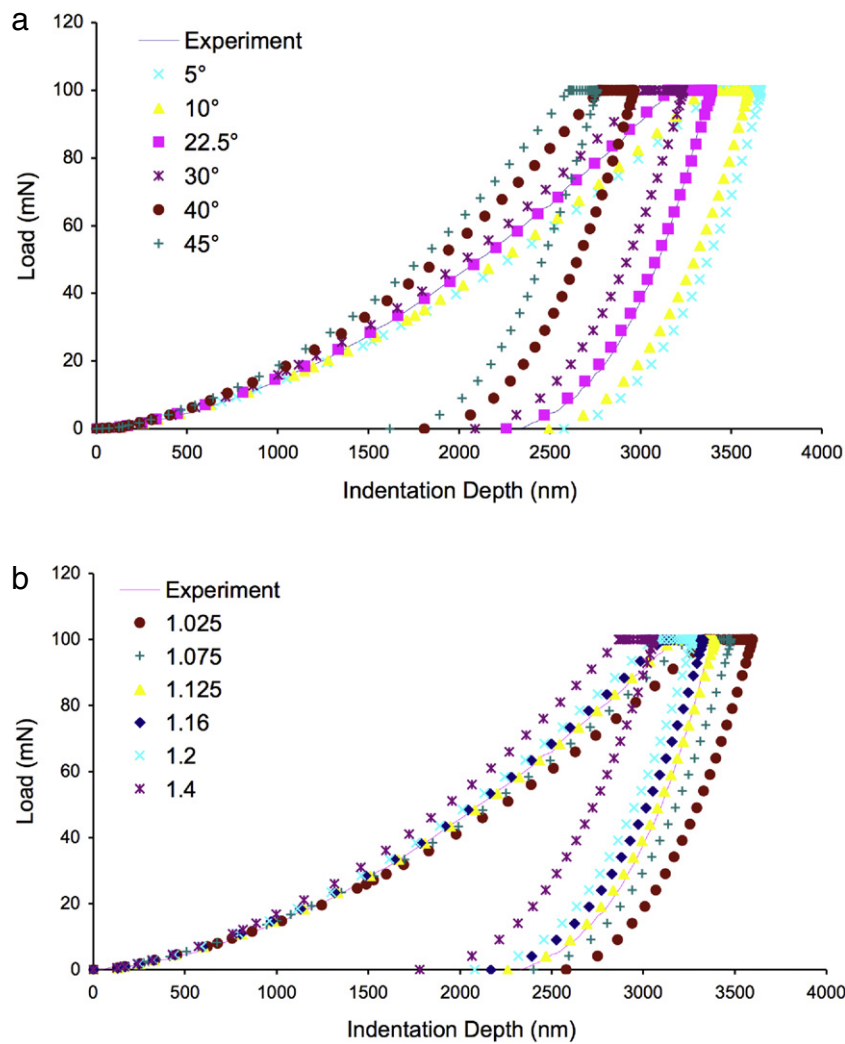


**Fig. 11 – Load vs. indentation depth curves, (a) as a function of  $\psi$ ; (b) as a function of  $\sigma_{b0}/\sigma_{c0}$ . Other parameter values taken from Table 1.**

preserves, to a greater extent, the original (undamaged) stiffness. Finally, as one decreases Young’s modulus, the IID also increases, reflecting the loss in contact stiffness.

Fig. 14(b) shows the sensitivity of the TCD to the simulation parameters. It can be seen that this characteristic is sensitive to all parameters, though to a lesser extent for  $\psi$ ,  $\beta$ , and  $\gamma$ . The parameters with the largest influence are  $E^{el}$ ,  $\sigma_{b0}/\sigma_{c0}$ ,  $\sigma_{c0}$ , and  $\mu$ . Decreasing  $\sigma_{c0}$  has a very strong effect, since the material begins yielding sooner and large (percentage) changes in creep displacement will occur. Similarly, as one decreases  $E^{el}$  and  $\mu$ , the TCD decreases, due to contact stiffening and decreased viscous (decreased time constant) effects, respectively.

Fig. 15(a) shows the sensitivity of the FID to the simulation parameters. It can be seen that this characteristic is sensitive to all parameters, with the exception of  $\mu$ , which is relatively insensitive. The parameters with the largest effect are  $\sigma_{b0}/\sigma_{c0}$ ,  $\sigma_{c0}$ ,  $\gamma$ , and  $E^{el}$ . Increasing  $\sigma_{b0}/\sigma_{c0}$  has a very strong effect, as it elevates the “effective” compressive yield stress under confined compression, creating a stiffening effect. A stiffer contact will then incur reduced FID. Similarly, as one

decreases the compressive yield stress, the FID increases, since plastic deformation (which has a softening effect) occurs to a greater extent during loading (and holding), which results in a larger FID. In addition, decreasing  $\gamma$  increases the FID. Again, with a smaller value of  $\gamma$ , the final value of  $d_c$  will also decrease; thus, a lesser amount of damage occurs, diminishing the rapid stiffness loss observed near the end of unloading. Finally, as one decreases Young’s modulus, the FID also decreases, reflecting the loss in contact stiffness (see Fig. 12(b)).

Fig. 15(b) shows the sensitivity of the FS to the simulation parameters. Again,  $\sigma_{b0}/\sigma_{c0}$ ,  $\sigma_{c0}$ , and  $E^{el}$  have a strong influence on this slope; however,  $\gamma$  exhibits the strongest effect. Since  $\gamma$  limits the reduction in the stiffness due to damage, smaller values can increase the FS by a large percentage.

#### 4. Discussion

Numerous hierarchical structural models for osteonal bone have been proposed in the literature (for example, see Lakes

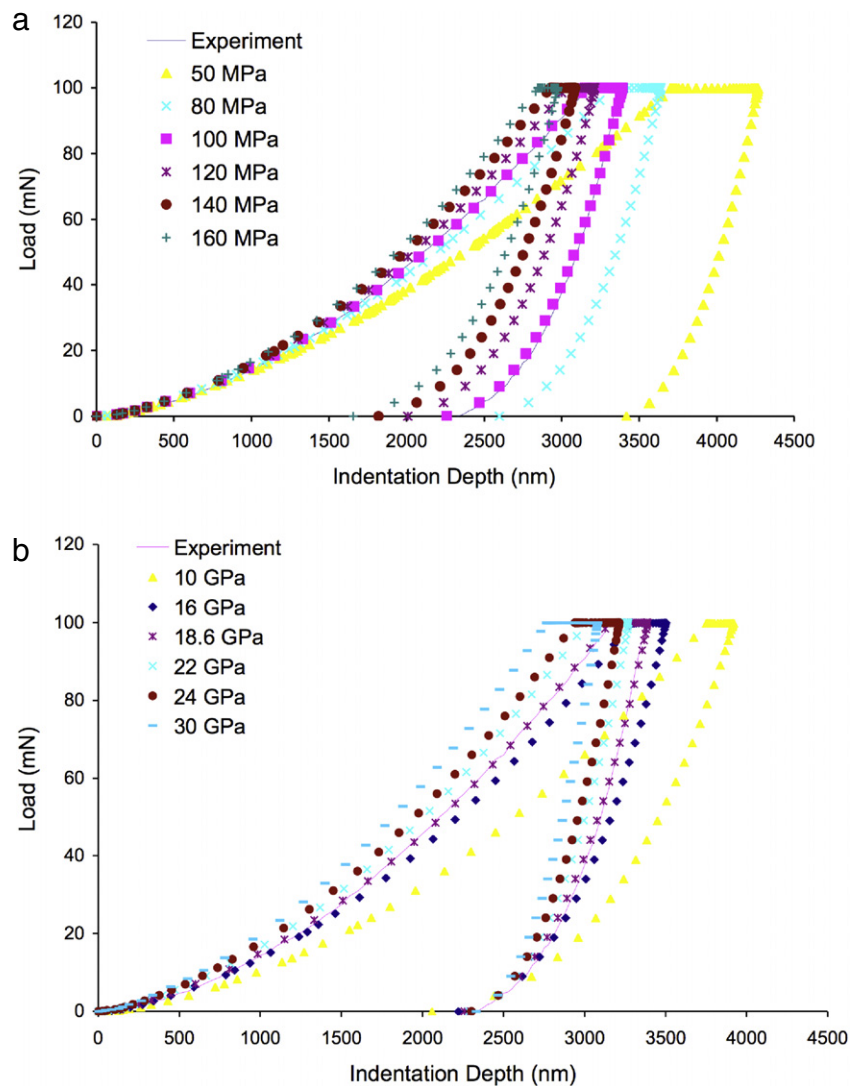


**Fig. 12 – Load vs. indentation depth curves, (a) as a function of  $\sigma_{c0}$ ; (b) as a function of  $E^{el}$ . Other parameter values taken from Table 1.**

(1993)). The models are similar in that they first define the structure of osteonal bone as originating from the double helix collagen molecule, with a length scale in the nm range, then progress to collagen fibrils (with interspersed hydroxyapatite crystals) on a scale of 100 nm. Next, the individual fibrils assemble into bundled collagen fibers, with a length scale in the 1  $\mu\text{m}$  range. These bundled collagen fibers form a series of concentric lamella structures (on the order of 10  $\mu\text{m}$ ) as individual Haversian osteons, close-packed (on the order of 200  $\mu\text{m}$ ) in a configuration similar to that of unidirectional fibers within a composite matrix. The concentric lamella contain osteocyte lacunae and canaliculi, which are void-like structural defects. This structural scale, on the order of 10  $\mu\text{m}$ , consisting of bundled collagen fibers, osteocyte lacunae, and canaliculi, is the pertinent scale of interest during micro-scale indentation. Evidence of this was shown in Fig. 8, a contour plot of the scalar damage variable,  $d_c$ , at the point of maximum indentation depth. Note that  $d_c$  is greatest nearest the tip of the indenter and decreases

both toward the edge of contact and at increasing depths, as expected.

The plastic-damage model was also used to correlate the measured stiffness reduction due to damage. The region directly beneath the indenter, which is the final region in contact with the indenter during unloading (Fig. 9, bottom), also displays an average  $d_c$  value in good agreement with the contact stiffness reduction noted previously. Based on these results, the incorporation of damage effects in addition to the previously-assumed elasto-plastic behavior seems to be essential to capture the characteristic response of bone during indentation, particularly during the latter stage of unloading. In this study, dehydrated samples were used, however, it should be noted that the final parameter values in the simulations would be expected to vary depending on the type of bone tested, its susceptibility to damage, and level of hydration.

In order to further investigate the results from the damage model simulations, bovine cortical bone indentation tests were performed. A typical indent cross section, partitioned

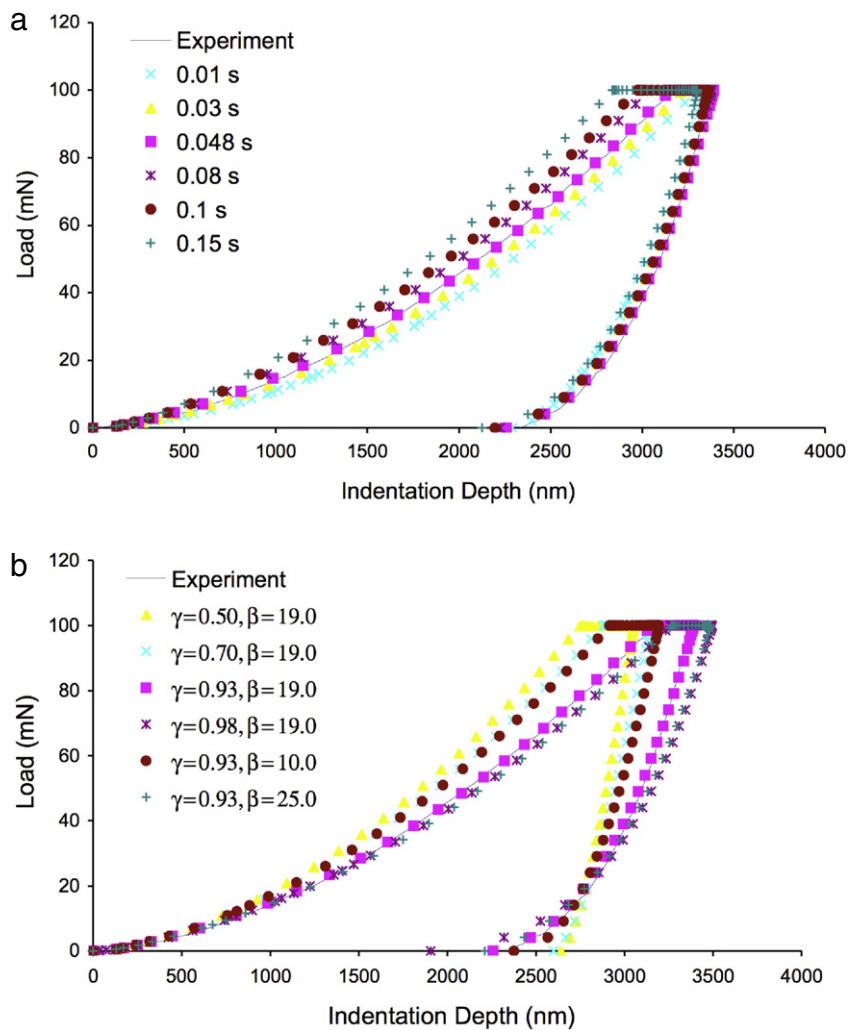


**Fig. 13 – Load vs. indentation depth curves, (a) as a function of  $\mu$ ; (b) as a function of  $\gamma$  and  $\beta$ . Other parameter values taken from Table 1.**

along the centerline of the indenter axis, can be seen in Fig. 10. Calcein stain labeling displayed qualitative agreement with the damage zone prediction in Fig. 9(bottom). However, it is questionable as to whether or not calcein stain labeling is capable of displaying a color gradient, on the micro-scale, that would result in the appearance of  $d_c$  contours in Figs. 8 or 9.

Changes in individual parameters, and the effect on the load vs. indentation depth curves, were also investigated. In general, the changes can be correlated to a generic “stiffening” or “softening” influence on the simulation curves. In addition, inference to a more rapid or slower onset of plastic deformation can also be used to interpret the results. Using the simplified plastic-damage model, a sensitivity analysis of the model parameters was also performed. The results showed that the model parameters exhibited a varying degree of influence on the indentation curve characteristics that were examined. The parameters that exhibited the greatest degree of influence were the compressive yield stress (contained in both  $\sigma_{b0}/\sigma_{c0}$  and  $\sigma_{c0}$ ), and Young’s modulus,  $E^{el}$ . The time constant,  $\mu$ , exhibited little influence with the exception of the total creep displacement. The parameter

$\gamma$  influenced the final indentation depth and final slope, which is not surprising given that it limits the scalar damage parameter  $d_c$ .

The question of the uniqueness of a parameter set is best proven mathematically, and given that this model contains seven parameters (eight including Poisson’s ratio), it is unlikely that a single set of parameters could be expected to uniquely reproduce one of the four indentation response curve characteristics examined in this study. However, as in all multi-parameter models (e.g., multi-scale hierarchical computational material models of anisotropic materials), the utility of any model rests in the ability to input values for parameters that have experimental justification and still obtain reasonable results. The values we selected in Table 1 are reasonable and in some cases match experimentally-determined literature values. Based on this, we feel that the simplified plastic-damage model is useful for simulating the mechanics of cortical bone indentation, and can capture trends and important features of the indentation response unlike any other model used previously in the literature.

Future work includes tracking of the damage variable,  $d_c$ , as a function of indentation depth and/or repeated

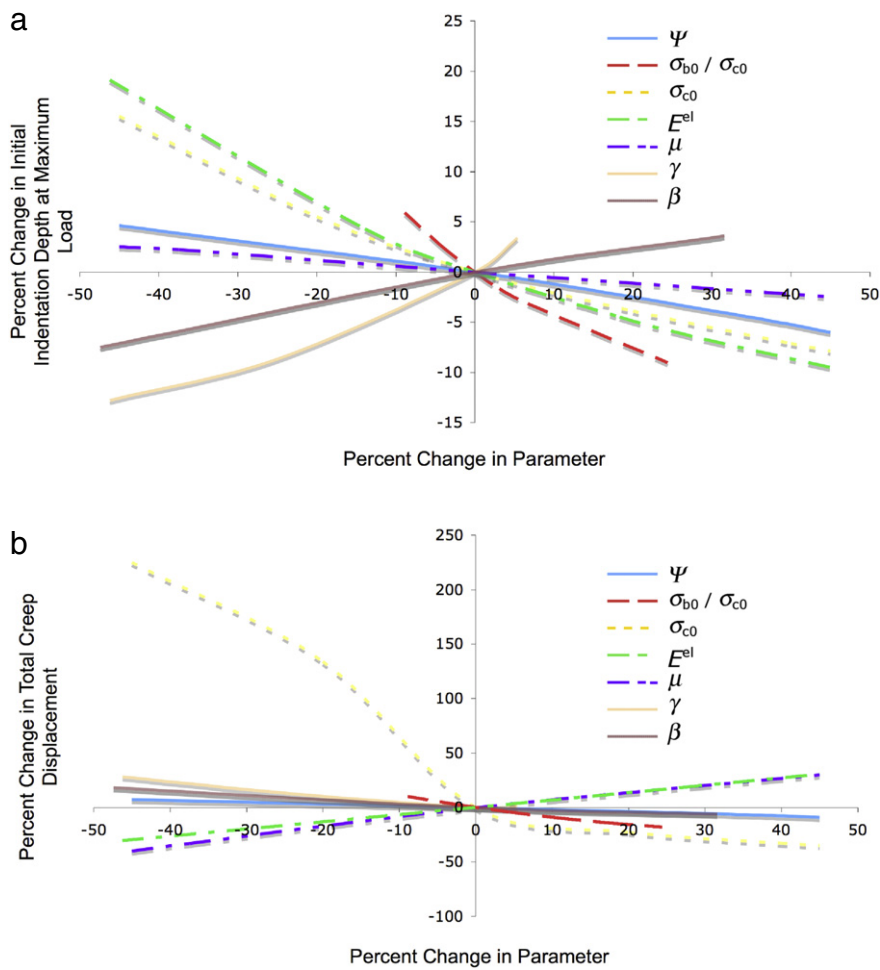


**Fig. 14 – Sensitivity results for simplified plastic damage model, (a) percent change in initial indentation depth at maximum load (IID) as a function of percentage change in model parameters; (b) percentage change in total creep displacement (TCD) as a function of percent change in model parameters.**

indentation cycles, and relating  $d_c$  to changes in modulus or stiffness throughout the loading/unloading cycles. Future areas of investigation also include more detailed examination of the micro-mechanical mechanisms of damage during indentation, as well as correlation of  $d_c$  with data on local bone mineral density in the region of the indents. Based on our preliminary studies, and the microstructural architecture of bone, we postulate that inelastic bone material properties are highly non-local. Similar to concrete and other microstructural cementitious materials, the experimentally-observed response is assumed to strongly depend on the size of the indenter and indentation speed, or, mathematically speaking, on the ratio between the microstructural length scale and the size of the damage zone (Mahnken and Kuhl, 1999; Gitman et al., 2008).

## 5. Conclusions

Indentation of bone has previously been assumed to result in both visco-elastic and plastic deformation. However, ordinary visco-elastic/plastic constitutive models based on linear or

power law plastic hardening are not able to capture the complete unloading response during indentation of bone, particularly near the end of unloading, due to the decrease in stiffness. We hypothesize that the constitutive response of bone during indentation testing can be characterized through an elasto-plastic damage model commonly used for cohesive frictional materials such as concrete, mortar, or rock.

Examination of the equivalent plastic strains in tension and compression for a (symmetric) elastic perfectly-plastic material model shows that tensile effects are localized primarily at the edge of contact and are an order of magnitude smaller than the equivalent plastic strains in compression, which are located directly beneath the indenter. This allows one to include only compressive damage to significantly reduce the parameter set.

A plastic-damage model, implemented via ABAQUS<sup>TM</sup>, using nominal values for its parameter set and an optimized curve relating the scalar damage variable,  $d_c$ , with the equivalent plastic strains,  $\kappa_c$ , exhibits good agreement with experimental data, particularly during unloading. A sensitivity analysis showed that the compressive yield stress, Young's modulus, and the limiting value of the scalar damage variable exhibited the strongest influence on the indentation

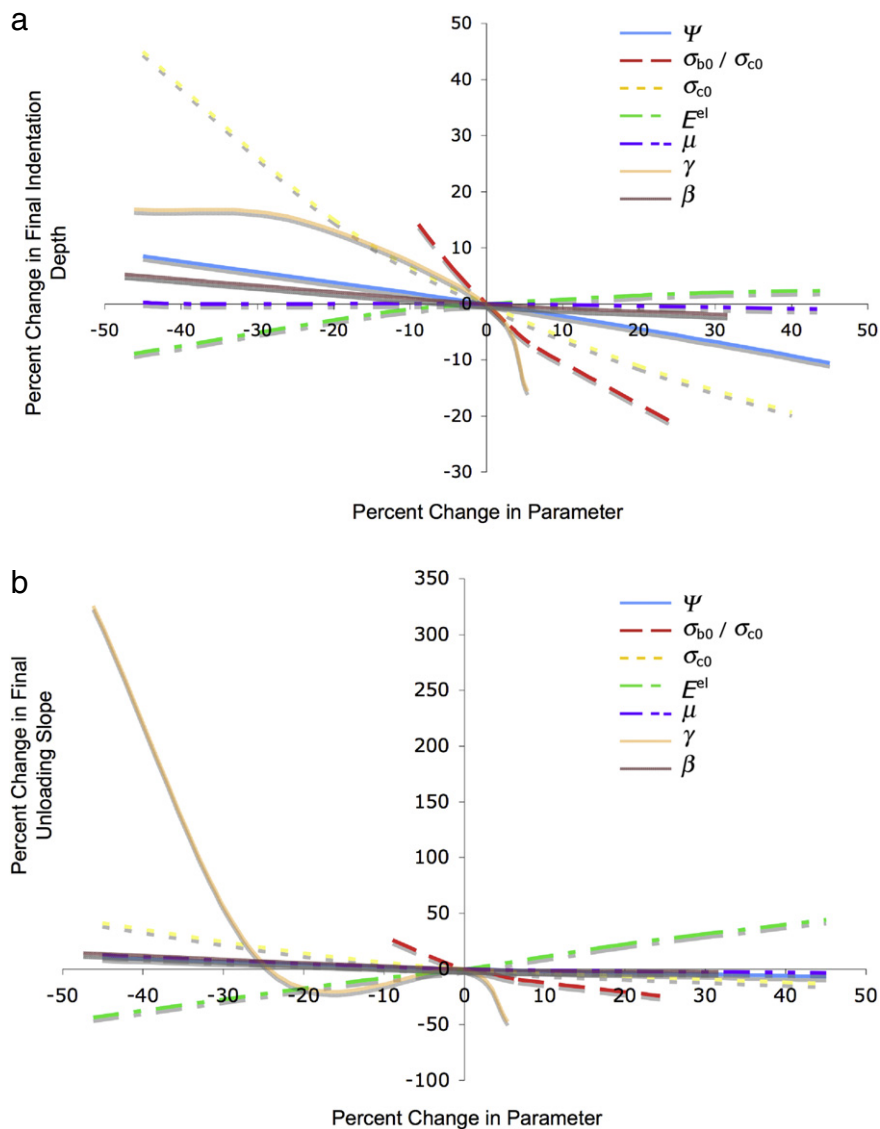


**Fig. 15 – Sensitivity results for simplified plastic damage model, (a) percentage change in final indentation depth (FID) as a function of percent change in model parameters; (b) percent change in final unloading slope (FS) as a function of percent change in model parameters.**

response curve characteristics examined here. The predicted stiffness degradation at the end of unloading, as a result of damage to bone at a microstructural level, is capable of explaining this characteristic in the unloading curve observed experimentally during the indentation of bone.

### Acknowledgments

The support of the NIH under grant R01 AR052008-01A1 is gratefully acknowledged. Its contents are solely the responsibility of the authors and do not necessarily represent the official views of the NIH. The authors would also like to acknowledge the support of Eli Lilly Company, and Dr. Charles Turner, Indiana University Depts. of Orthopaedic Surgery and Biomedical Engineering.

### REFERENCES

- Archdeacon, M.T., Jepsen, K.J., Davy, D.T., 1996. The effects of torsional loading conditions and damage on bovine cortical bone strength. In: Proceedings of the Fifteenth Southern Biomedical Engineering Conference, Dayton, OH. pp. 445–448.
- Carter, D.R., Caler, W.E., 1985. A cumulative damage model for bone fracture. *Journal of Orthopaedic Research* 3, 84–90.
- Carter, D.R., Hayes, W.C., 1977. Compact bone fatigue damage — I. Residual strength and stiffness. *Journal of Biomechanics* 10, 325–337.
- Chollacoop, N., Dao, M., Suresh, S., 2003. Depth-sensing instrumented indentation with dual sharp indenters. *Acta Materialia* 51, 3713–3729.
- Contrafatto, L., Cuomo, M., 2006. A framework of elastic–plastic damaging model for concrete under multiaxial stress states. *International Journal of Plasticity* 22, 2272–2300.

- Dao, M., Challacoop, N., Van Vliet, K.J., Venkatesh, T.A., Suresh, S., 2001. Computational modeling of the forward and reverse problems in instrumented sharp indentation. *Acta Materialia* 49, 3899–3918.
- Das, G., Das, M., Sinha, S., Gupta, K., Chakrabarty, S., Ray, A., 2009. Characterization of cast stainless steel weld pools by using ball indentation technique. *Materials Science and Engineering: A* 513–514, 389–393.
- Enoki, M., Kishi, T., 1991. Development and future aspects of AE source characterization. In: *Acoustic Emission: Current Practice and Future Directions*. STP 1077. American Society for Testing and Materials, Philadelphia, PA. pp. 47–66.
- Fan, Z., Rho, J.Y., Swadener, J.G., 2004. Three-dimensional finite element analysis of the effects of anisotropy on bone mechanical properties measured by nanoindentation. *Journal of Materials Research* 19, 114–123.
- Fischer, R.A., Arms, S.W., Pope, M.H., Seligson, D., 1986. Analysis of the effect of using two different strain rates on the acoustic emission in bone. *Journal of Biomechanics* 19, 119–127.
- Frost, H.L., 1960. Presence of microscopic cracks *in vivo* in bone. *Henry Ford Hospital Medical Bulletin* 8, 25–35.
- Garcia, D., Zysset, P.K., Charlebois, M., Curnier, A., 2009. A three-dimensional elastic–plastic damage constitutive law for bone tissue. *Biomechanics and Modeling in Mechanobiology* 8, 149–165.
- Gitman, I., Askes, H., Sluys, L.J., 2008. Coupled-volume multi-scale modeling of quasibrittle materials. *European Journal of Mechanics A/Solids* 27, 302–327.
- Grassl, P., Jirasek, M., 2006. Damage-plastic model for concrete failure. *International Journal of Solids and Structures* 43, 7166–7196.
- Hägglund, R., Isaksson, P., 2007. Influence of damage in the vicinity of a crack-tip in embossed low-basis-weight paper. *Engineering Fracture Mechanics* 74, 1758–1769.
- Hansen, U., Zioupos, P., Simpson, R., Currey, J.D., Hynd, D., 2008. The effect of strain rate on the mechanical properties of human cortical bone. *ASME Transactions, Journal of Biomechanical Engineering* 130, 011011-1–011011-8.
- Hart, R.T., Davy, D.T., Heiple, K.G., 1984. A computational method for stress analysis of adaptive elastic materials with a view toward applications in strain induced bone remodeling. *ASME Transactions, Journal of Biomechanical Engineering* 106, 342–350.
- Hoffler, C.E., Guo, X.E., Zysset, P.K., Goldstein, S.A., 2005. An application of nanoindentation technique to measure bone tissue lamellae properties. *ASME Transactions, Journal of Biomechanical Engineering* 127, 1046–1053.
- Inoue, S., Sakakida, K., Yamasita, F., Kusakabe, T., Inoue, N., 1986. Acoustic emission characteristics of the cortical bone under tensile loading. *Progress in Acoustic Emission III*, Japanese Society of NDI. p. 244.
- Jepsen, K.J., Davy, D.T., 1997. Comparison of damage accumulation measures in human cortical bone. *Journal of Biomechanics* 30, 891–894.
- Johnson, K.L., 1985. *Contact Mechanics*. Cambridge Press, New York.
- Jonsson, U., Eriksson, K., 1984. Microcracking in dog bone under load: A biomechanical study of bone visco-elasticity. *Acta Orthopaedica Scandinavica* 55, 441–447.
- Kachanov, L.M., 1986. *Introduction to Continuum Damage Mechanics*. Martinus Nijhoff, Dordrecht.
- Kachanov, L.M., 1958. On the time to failure under creep conditions. *Izvestiia Akademii Nauk SSSR Otdelenie Tekhnika Nauk* 8, 26–31.
- Keaveny, T.M., Wachtel, E.F., Guo, X.E., Hayes, W.C., 1994. Mechanical behavior of damaged trabecular bone. *Journal of Biomechanics* 27, 1309–1318.
- Kohn, D.H., 1995. Acoustic emission and nondestructive evaluation of biomaterials and tissues. *Critical Reviews in Biomedical Engineering* 22, 221–306.
- Kotha, S.P., Guzelsu, N., 2003. Tensile damage and its effects on cortical bone. *Journal of Biomechanics* 36, 1683–1689.
- Lakes, R., 1993. Materials with structural hierarchy. *Nature* 361, 511–515.
- Lee, J., Jang, J., Lee, B., Choi, Y., Lee, S., Kwon, D., 2006a. An instrumented indentation technique for estimating fracture toughness of ductile materials: A critical indentation energy model based on continuum damage mechanics. *Acta Materialia* 544, 1101–1109.
- Lee, J., Kim, K., Kwon, D., Kim, D., 2006b. Evaluation of fracture toughness using indentation method based on continuum damage mechanics. In: *Proceedings of the International Offshore and Polar Engineering Conference*. pp. 81–85.
- Lee, K., Kim, H., Park, S., Lee, J., Kim, K., Kwon, D., 2008. Nondestructive estimation of fracture toughness using instrumented indentation technique. *Key Engineering Materials* 385–387, 893–896.
- Lee, J., Fenves, G.L., 1998. Plastic-damage model for cyclic loading of concrete structures. *Journal of Engineering Mechanics* 124, 892–900.
- Lees, C.J., Register, T.C., Turner, C.H., Wang, T., Stancill, M., Jerome, C.P., 2002. Effects of raloxifene on bone density, biomarkers, and histomorphometric and biomechanical measures in ovariectomized cynomolgus monkeys. *Menopause: The Journal of the North American Menopause Society* 9, 320–328.
- Lemaitre, J., Chaboche, J.L., 1990. *Mechanics of Solid Materials*. Cambridge University Press, Cambridge.
- Licht, V., Ernst, E., Huber, N., 2003. Simulation of the Hertzian contact damage in ceramics. *Modelling and Simulation in Materials Science and Engineering* 11, 477–486.
- Lubliner, J., Oliver, J., Oller, S., Oñate, E., 1989. A plastic-damage model for concrete. *International Journal of Solids and Structures* 25, 229–326.
- Mahnken, R., Kuhl, E., 1999. Parameter identification of gradient enhanced damage models with the finite element method. *European Journal of Mechanics/A: Solids* 18, 819–835.
- Martin, R.B., Burr, D.B., 1982. A hypothetical mechanism for the stimulation of osteonal remodeling by fatigue damage. *Journal of Biomechanics* 15, 137–139.
- Menzel, A., Ekh, M., Runesson, K., Steinmann, P., 2005. A framework for multiplicative elastoplasticity with kinematic hardening coupled to anisotropic damage. *International Journal of Plasticity* 21, 397–434.
- Mullins, L.P., Bruzzi, M.S., McHugh, P.E., 2009. Calibration of a constitutive model for the post-yield behaviour of cortical bone. *Journal of the Mechanical Behavior of Biomedical Materials* 2, 460–470.
- Niebur, G.L., Feldstein, M.J., Yuen, J.C., Chen, T.J., Keaveny, T.M., 2000. High-resolution finite element models with tissue strength asymmetry accurately predict failure of trabecular bone. *Journal of Biomechanics* 33, 1575–1583.
- Niebur, G.L., Yuen, J.C., Burghardt, A.J., Keaveny, T.M., 2001. Sensitivity of damage predictions to tissue level yield properties and apparent loading conditions. *Journal of Biomechanics* 34, 699–706.
- O'Brien, F.J., Taylor, D., Lee, T.C., 2003. Microcrack accumulation at different intervals during fatigue testing of compact bone. *Journal of Biomechanics* 36, 973–980.
- Ovaert, T.C., Kim, B.R., Wang, J., 2003. Multi-parameter models of the viscoelastic/plastic mechanical properties of coatings via combined nanoindentation and non-linear finite element modeling. *Progress in Organic Coatings* 47, 312–323.
- Pelled, G., Tai, K., Sheyn, D., Zilberman, Y., Kumbar, S., Nair, L.S., Laurencin, C.T., Gazit, D., Ortiz, C., 2007. Structural and nanoindentation studies of stem cell-based tissue-engineered bone. *Journal of Biomechanics* 40, 399–411.

- Phillips, A.T.M., Pankaj, P., Usmani, A.S., Howie, C.R., 2003. The effect of bone graft bed depth on the short term stability of revision hip arthroplasty: A finite element investigation. *European Cells and Materials* 6, 23.
- Prendergast, P.J., Huiskes, R., 1996. Finite element analysis of fibrous tissue morphogenesis—A study of the osteogenic index using a biphasic approach. *Mechanics of Composite Materials* 32, 209–218.
- Ramtani, S., Zidi, M., 2001. A theoretical model of the effect of continuum damage on a bone adaptation model. *Journal of Biomechanics* 34, 471–479.
- Reifsnider, K.L., 1991. Damage and damage mechanics. In: Reifsnider, K.L. (Ed.), *Fatigue of Composite Materials*. Elsevier, New York, pp. 11–77.
- Sun, X., Khaleel, M., 2004. Modeling of glass fracture damage using continuum damage mechanics — Static spherical indentation. *International Journal of Damage Mechanics* 13, 263–285.
- Sun, X., Khaleel, M., Davies, R., 2005. Modeling of stone-impact resistance of monolithic glass ply using continuum damage mechanics. *International Journal of Damage Mechanics* 14, 165–178.
- Tai, K., Ulm, F.-J., Ortiz, C., 2006. Nanogranular origins of the strength of bone. *Nano Letters* 6, 2520–2525.
- Tai, K., Qi, H.J., Ortiz, C., 2005. Effect of mineral content on the nanoindentation properties and nanoscale deformation mechanisms of bovine tibial cortical bone. *Journal of Materials Science: Materials in Medicine* 16, 947–959.
- Vashishth, D., Kim, D., Rho, J., 2002. The Influence of tensile and compressive damage on bending fatigue of human cortical bone. In: *Proceedings of the Second Joint EMBS/BMES Conference*, Houston, TX.
- Wang, J., Ovaert, T.C., 2009. Computational mechanical property determination of viscoelastic/plastic materials from nanoindentation creep test data. *Journal of Materials Research* 24, 1230–1242.
- Wright, T.M., Vosburgh, F., Burstein, A.H., 1981. Permanent deformation of compact bone monitored by acoustic emission. *Journal of Biomechanics* 14, 405–409.
- Zhang, J., Niebur, G.L., Ovaert, T.C., 2008. Mechanical property determination of bone through nano- and micro-indentation testing and finite element simulation. *Journal of Biomechanics* 41, 267–275.
- Zysset, P.K., Guo, X.E., Hoffler, C.E., Moore, K.E., Goldstein, S.A., 1999. Elastic modulus and hardness of cortical and trabecular bone lamellae measured by nanoindentation in the human femur. *Journal of Biomechanics* 32, 1005–1012.